Chemical Engineering Journal 417 (2021) 128552

Contents lists available at ScienceDirect

Chemical Engineering Journal

journal homepage: www.elsevier.com/locate/cej

# Shape matters: $SnP_{0.94}$ teardrop nanorods with boosted performance for potassium ion storage

Chun-Yu Tsai [1], Chao-Hung Chang [1], Tzu-Lun Kao, Kuan-Ting Chen, Hsing-Yu Tuan

*Department of Chemical Engineering, National Tsing Hua University, Hsinchu 30013, Taiwan*

ARTICLE INFO

*Keywords:*
Tin phosphide
Teardrop nanorods
Supercritical fluid-liquid-solid
Morphology-dependence
Potassium ion batteries
Anodes

ABSTRACT

Benefit from the unique structural characteristics of polymeric cross-linkage crystal with large interlayer spacing, $SnP_{0.94}$ has been regarded as an appropriate dual conversion-alloying anode material, providing symmetric high-speed ion diffusion tunnels perpendicular to the *c*-axis of the hexagonal lattice. However, the critical issue of volume change stemming from fully alloying-dealloying reaction still need to be challenged. We report the first example of uniform $SnP_{0.94}$ teardrop nanorods by utilizing bismuth (Bi) as a seed through the one-pot synthesis method in supercritical organic solvent. The Bi-seed $SnP_{0.94}$ teardrop nanorod anode exhibited a high reversible capacity of 422.8 mA h $g^{-1}$ at 50 mA $g^{-1}$ and excellent rate performance (285.8 mA h $g^{-1}$ at 1000 mA $g^{-1}$), which is superior to the other reported $SnP_{0.94}$ nanomaterials. Based on the results of electrochemical impedance spectroscopy (EIS) assisted with *ex-situ* transmission electron microscope (TEM) and *ex-situ* X-ray photoelectron spectroscopy (XPS), teardrop-shaped nanostructures can more effectively relieve the surface tension, alleviate the expansion, and maintain structural stability during cycling than spherical particles with similar sizes, demonstrating strong evidence on its shape effects on electrochemical performance. Finally, the potassium ion batteries with $SnP_{0.94}$ teardrop nanorods (designated as T-SnP) as an anode and perylenetetracarboxylic dianhydride (PTCDA) as a cathode to full cells delivered a long cycling life of up to 450 cycles at a current density of 1000 mA $g^{-1}$, moreover, a pouch-type battery is also fabricated for feasible demonstration for its practical application.

## 1. Introduction

Potassium ion batteries (PIBs) have highly attracted tremendous attention system as a promising alternative metal ion battery to lithium ion battery (LIBs) in recent years. Considering the possible exhaustion of lithium (Li) feedstock and the significant increase in demand for battery-embedded portable devices, potassium (K) combines the merits of the abundant reserves and relatively low costs [1,2]. The standard redox potential of $K^+/K$ (−2.93 V vs. $E_o$) is almost as low as that of $Li^+/Li$ (−3.04 V vs. $E_o$), and due to smaller solvation ions and fast ionic conductivity in aqueous electrolyte, it demonstrates a further favorable condition to consider PIBs as a large-scale integration of energy storage in the grid [3,4]. Carbonaceous materials are industrially recognized anode material in LIBs in terms of low cost and high conductivity, and have been initially investigated as PIB anode materials [5–11]. In addition, the inherent doping elements of biomass-derived carbon can even enhance the ion adsorption [12]. However, since the ionic radius of K ions is larger than that of Li ions ($K^+$, 1.38 Å vs. $Li^+$, 0.76 Å), the formation of $KC_8$ phase (theoretical capacity of 279 mA h $g^{-1}$) suffers a lot of volume expansion, which is due to the large amount of K ions into the carbon layer, causing the structure to be drastically destroyed. Irreversible capacity will be caused by repeated potassiation/depotassiation processes, resulting in poor electrochemical performance [13].

In order to increase the energy density without sacrificing long cycle life, many possible electrode materials for PIBs have been proposed [14–20]. Among the reported elements, phosphorus (P) has the highest theoretical gravimetric capacity of 865 mA h $g^{-1}$ corresponding to the KP phase which is much higher than that of carbonaceous materials ($KC_8$, 279 mA h $g^{-1}$). However, the poor intrinsic electrical conductivity and large P volume change make it difficult to reach the theoretical value of electrochemical performance in terms of utilization [21]. Even if a conductive carbon matrix has been carried out to facilitate charge transfer, the improvement in overall energy density is still not obvious.

Metal phosphide materials can promote a synergistic effect to both enhance electronic conductivity and tolerate the volume expansion [22,23]. Based on the dual conversion alloy mechanism, metal

*E-mail address:* hytuan@che.nthu.edu.tw (H.-Y. Tuan).
[1] These authors contributed equally to this work.

https://doi.org/10.1016/j.cej.2021.128552
Received 10 November 2020; Received in revised form 31 December 2020; Accepted 12 January 2021
Available online 18 January 2021

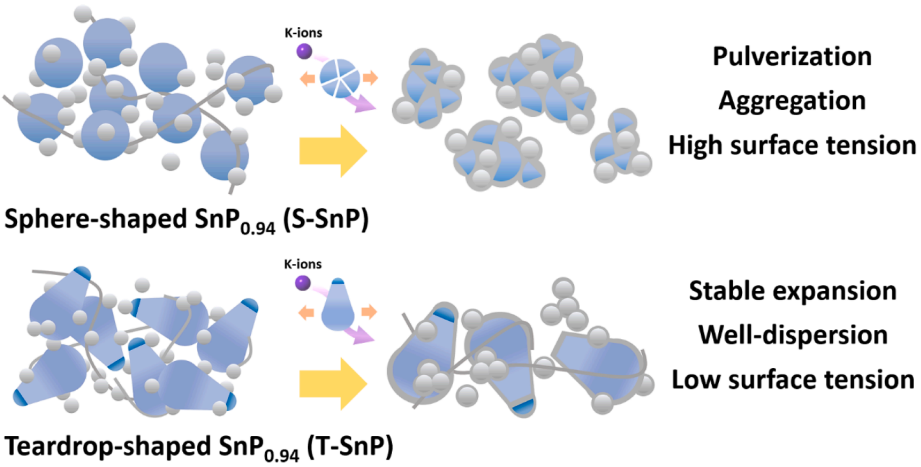


**Scheme 1.** Graphical abstract. Teardrop-shaped $SnP_{0.94}$ nanorods (T-SnP) effectively suppress the volume expansion and exhibit an anti-pulverization nanostructure without severe aggregation.

phosphide materials can deliver higher energy density, moreover, and can offset the above-mentioned undesirable problems [24]. The combinations of tin (Sn) and P in tin phosphide have been studied as attractive anode materials, such as $SnP_3$ [25], $Sn_4P_3$ [26], and $SnP_{0.94}$ [27], providing high theoretical gravimetric capacity and excellent rate capability in PIBs. Among them, $SnP_{0.94}$ has been proven to have high reversibility thanks to the layered structure of ion diffusion in LIBs and sodium ion batteries (SIBs) [28,29]. Meanwhile, the incorporation of the P phase and the KP phases that are repeatedly transferred during the cycle can prevent agglomeration and disperse mechanical stress to inhibit phase segregation [30]. Nevertheless, despite the enhanced buffering effect, huge volume changes still exist. Current research on tin phosphides in PIBs has been motivated to tackle this problem with a strategy to modify structure features [31,32]. Promoted by carbonaceous materials, tin phosphides can demonstrate advanced phase stability in cycling performance, even reaching to the $K_3P$ phase with improved electrochemical performances. Additionally, the side reaction at the electrode/electrolyte interface also poses a high impact in phosphorus-based anode of PIBs [33,34]. Zhang *et al.* focus on the electrolyte effect toward the SEI formation, and it has been confirmed that the salt and solvent used for electrolyte would highly change the composition of SEI based on the XPS analysis. Through electrolyte salt and solvent chemistry, the utilization of potassium trifluoromethanesulfonimide (KFSI) can construct more suitable SEI layer to reinforce the stability in PIBs owing to the most negative value of solvation energy [35,36]. Even though, the basic concept of shape-controlled to the tin phosphide nanostructures in PIBs has not been concluded explicitly.

In LIBs, the topic of volume changes in crystalline silicon-based materials has been explored comprehensively [37–39]. Lee *et al.* studied the volume expansion mechanism of silicon nanopillars, and it was found that the anisotropic expansion directions is based on the insertion/extraction of Li ions in a specific lattice plane [40]. Thereafter, Jung *et al.* computed and compared the interfacial energies of the lattice facets. Through the use of first-principles molecular dynamics calculation, the simulation results are consistent with the experimental observation, which provides strong evidence for the lattice-oriented speculation [41]. On the other hand, morphology characteristics are also expected to adjust the surface tension distribution caused by volume expansion [42]. The tunable shape of nanomaterials can address the problems of structural pulverization and solid-electrolyte interphase (SEI) reformation, thereby extending the stability and reversibility during cycling [43–45]. Klankowski *et al.* reported a bat-like core–shell heterostructure of silicon nanowires, which can demonstrate reversible structural changes and exhibit an anti-pulverization nanostructure [46]. Therefore, previous studies have concluded that due to lower lateral tension and mechanical degradation, one-dimensional nanostructures have better capacity to withstand volume expansion [47]. However, it is still not clear about the co-effects arising from the internal crystal facets and external surface morphologies.

Herein, we show the superior rate performance and stable cycling performance of $SnP_{0.94}$ teardrop nanorods for high performance PIBs based on a morphological approach. We report a supercritical fluid-liquid-solid (SFLS) method to synthesize the teardrop shapes of $SnP_{0.94}$ seeded with bismuth (Bi) nanoparticles through reasonable morphological controlling. The inherent crystal structure of $SnP_{0.94}$ teardrop provides not only diffusion tunnels between the interlayers along the largest spacing direction, but also high specific capacity among metal phosphides. The comparison of obtained $SnP_{0.94}$ teardrop nanorods (designated as T-SnP) and $SnP_{0.94}$ sphere nanoparticles (designated as S-SnP) exhibited the obvious improved cycling stability as anode for PIBs as shown in Scheme 1. The T-SnP anode exhibited a high reversible capacity of 422.8 mA h $g^{-1}$ at 50 mA $g^{-1}$ and excellent rate performance (285.8 mA h $g^{-1}$ at 1000 mA $g^{-1}$). This performance is better than all currently reported $SnP_{0.94}$ nanomaterials. Furthermore, the post-mortem analyses, such as *ex-situ* transmission electron microscope (TEM) and *ex-situ* X-ray photoelectron spectroscopy (XPS) of T-SnP, have been conducted to reveal the morphology evolution on electrochemical properties and elucidate the fundamental mechanisms conducting with electrochemical impedance spectroscopy (EIS). Finally, the coin-type and pouch-type full batteries with T-SnP as anodes and perylenetetracarboxylic dianhydride (PTCDA) as cathodes have also been manufactured and used for feasibility demonstrations in practical applications.

## 2. Results and discussion

The synthesis method of $SnP_{0.94}$ nanostructures is a one-pot batch reaction for nanocrystal growth *via* the SFLS mechanism. The dispersion solution of Bi crystals was obtained by dissolving bismuth 2-ethylhexanoate in oleylamine with bis[bis(trimethylsilyl)amino] tin (II) in molar ratio of 1:85 as well as certain amount of trioctylphosphine. After added sequentially into a titanium metallic reactor, the solution was heated to 425 °C to fully react state, while toluene was used as a supercritical fluid solvent [48]. The morphology of the product was controlled by adjusting reaction temperature and the addition of Bi crystals to generate sphere-shaped nanoparticles in the 0-D growth and teardrop-shaped nanorods from Bi seeds in the 1-D growth, respectively.

The crystal structures of the prepared $SnP_{0.94}$ samples is shown in Figure S1. Sn atoms and P atoms can form a 2D layered structure like a

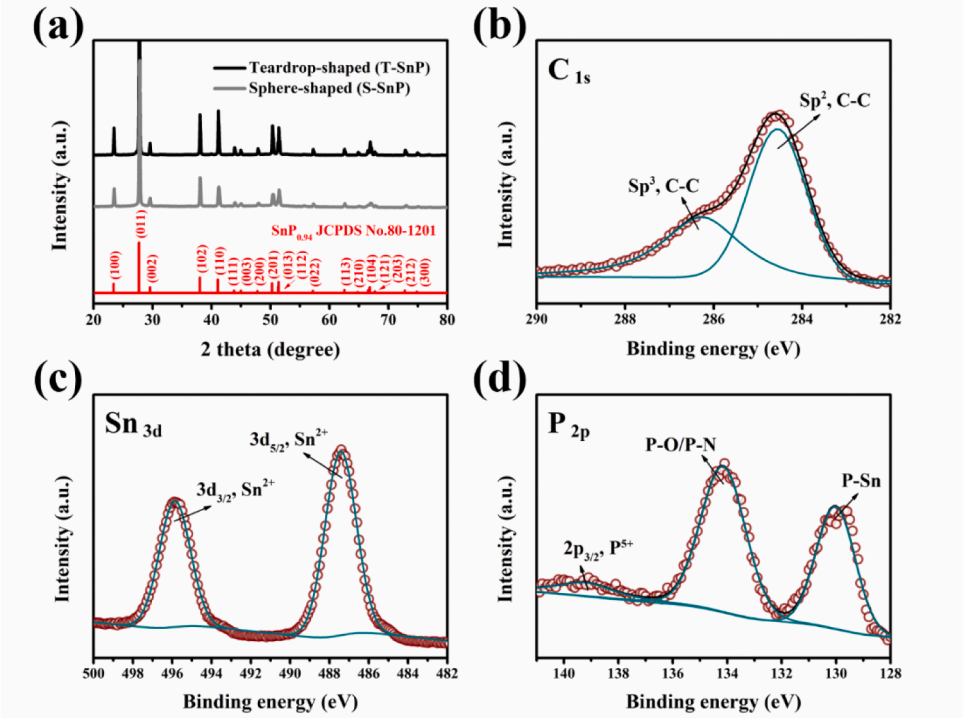


**Fig. 1.** (a) XRD pattern of the as-prepared $SnP_{0.94}$ nanomaterials. XPS spectrums of T-SnP in (b) C 1 s, (c) Sn 3d, and (d) P 2p, respectively.

polymeric cross-linkage [49]. The crystallinity and the purity of the product phase were identified by X-ray diffraction (XRD), and all the diffraction peaks of the two samples could be well marked as the crystal phase labeled as hexagonal $SnP_{0.94}$ (JCPDS NO. 80–1201) (Fig. 1a). To understand the chemical state of T-SnP, the element characteristics can be analyzed by X-ray photoelectron spectroscopy (XPS). A full scan of the spectrum showed the presence of Sn, P, and certain elements, which can be attributed to the surfactant ligand attached to the nanomaterials (Figure S2a). Two distinct peaks were observed in the C 1 s spectrum: 284.8 eV and 286.1 eV, corresponding to the $Sp^2$ and $Sp^3$-hybridized carbon, respectively (Fig. 1b). In the Sn 3d spectrum, only the distinct peaks of $Sn^{2+}$ at 487.4 eV and 495.7 eV can be clearly distinguished. It can be considered that this is a hexagonal stacked crystal formed by the Sn-P bonding structure [50], and there is no other deconvoluted peaks of $Sn^0$ and $Sn^{4+}$ (Fig. 1c). Specifically, several distinct peaks in the P 2p spectrum are located at 129.9 eV, 134.1 eV and 139.2 eV (Fig. 1d). It can be considered that the peak at 129.9 eV forms a P-Sn bond consistent with Sn 3d peaks, while the P-O and P-N bonds appearing at 134.1 eV are derived from ligands with surfactants. The peak at 139.2 eV is mainly based on the formation of slightly oxidized phosphorus on the surface of the nanorods. This result is consistent with the P-O bond formed by different peaks in the O 1 s region in the full scan of the spectrum (Figure S2a). It can be inferred that the sample is not easily oxidized during the synthesis process under the condition of water- and oxygen-free environment. The XPS spectrum of Bi contains four distinct peaks, which are 4f core splitting into Bi $4f_{5/2}$ and Bi $4f_{7/2}$. The valence states of Bi $4f_{5/2}$ at 164.4 eV and Bi $4f_{7/2}$ at 159.2 eV are originated from the oxides on the surface of Bi seeds (Figure S9a). Despite there is no obvious diffraction peak of Bi in XRD pattern, the content percentage of each element has been calculated by integration the peak area of XPS results in Table S1, indicating the low amounts of Bi in T-SnP.

The surface morphologies of the two prepared products were characterized by field emission scanning electron microscope (FESEM) and high-resolution transmission electron microscope (HRTEM). As shown in Fig. 2a and 2b, at the synthesis temperature of 480 °C, due to the higher reaction temperature, a nucleated phase may grow from the surface of seed crystals. On the other hand, Fig. 2c and 2d show that the lower reaction temperature of 425 °C causes the nucleation phase to grow along the specific crystal facet with the lowest surface energy. The resulting teardrop nanorods have a uniform spherical shape with an average *c*-axis length of about 200 nm. Although the diameter of the formed nanostructures varies along the axial direction, the synthesis mechanism of the teardrop shape can still be regarded as previous studies on nanopillars and nanorods [51,52]. The HRTEM image of T-SnP reveals a single crystal structure with excellent crystallinity (Fig. 2e and 2f). Fast Fourier transforms (FFT) analyses show that the tip part is crystalline Bi with a zone axis of [0 1 0] while the body part is $SnP_{0.94}$ with a zone axis of [0 1 0]. Moreover, the pattern of the body part contains fringes between the diffraction points, and these fringes are stacking defects of crystals in the axial direction. Therefore, the main growth direction of $SnP_{0.94}$ is determined to be [0 0 1], and its lattice spacing is 0.60 nm, which is consistent with the diffraction peak in XRD. The elemental composition ratio of the sample can be confirmed by energy dispersive X-ray spectroscopy (EDS). The T-SnP was uniformly composed of Sn, P, and Bi seeds. The atomic ratio of the tip and the body part is listed (Fig. 2g and 2 h), indicating that the ratio between tin and phosphorus is almost 1:1.

The electrochemical behaviors of potassium ion storage were evaluated in a coin-type CR2032 half-cell with potassium metal as the counter electrode. The electrode slurry is prepared in a stainless steel tank through a one-pot wet ball milling (WBM) process [19]. Figure S3 shows the SEM image of a mixture of T-SnP electrode slurry, $SnP_{0.94}$, ketjen black (KB), multi-walled carbon nanotube (MWCNT), and sodium carboxymethylcellulose (NaCMC) by WBM. It can be clearly observed that the T-SnP did not break and maintained its original morphology. According to previous studies on the electrolyte effect of the SEI layer, it has been proven that concentrated electrolyte based on KFSI can improve the cycle stability of PIBs [53,54]. Similarly, the inert nature of dimethoxyethane (DME) can be used as a solvent to reduce the reactivity of the SEI layer [55]. Thus, high-concentrated KFSI-DME electrolyte was selected for the electrochemical analyses (Fig. 3).

Fig. 3a shows the cyclic voltammetry (CV) curve of T-SnP in the potential range of 0.05 to 2.0 V with a scan rate of 0.1 mV $s^{-1}$. In addition, the CV curve of S-SnP is presented in Figure S4, providing

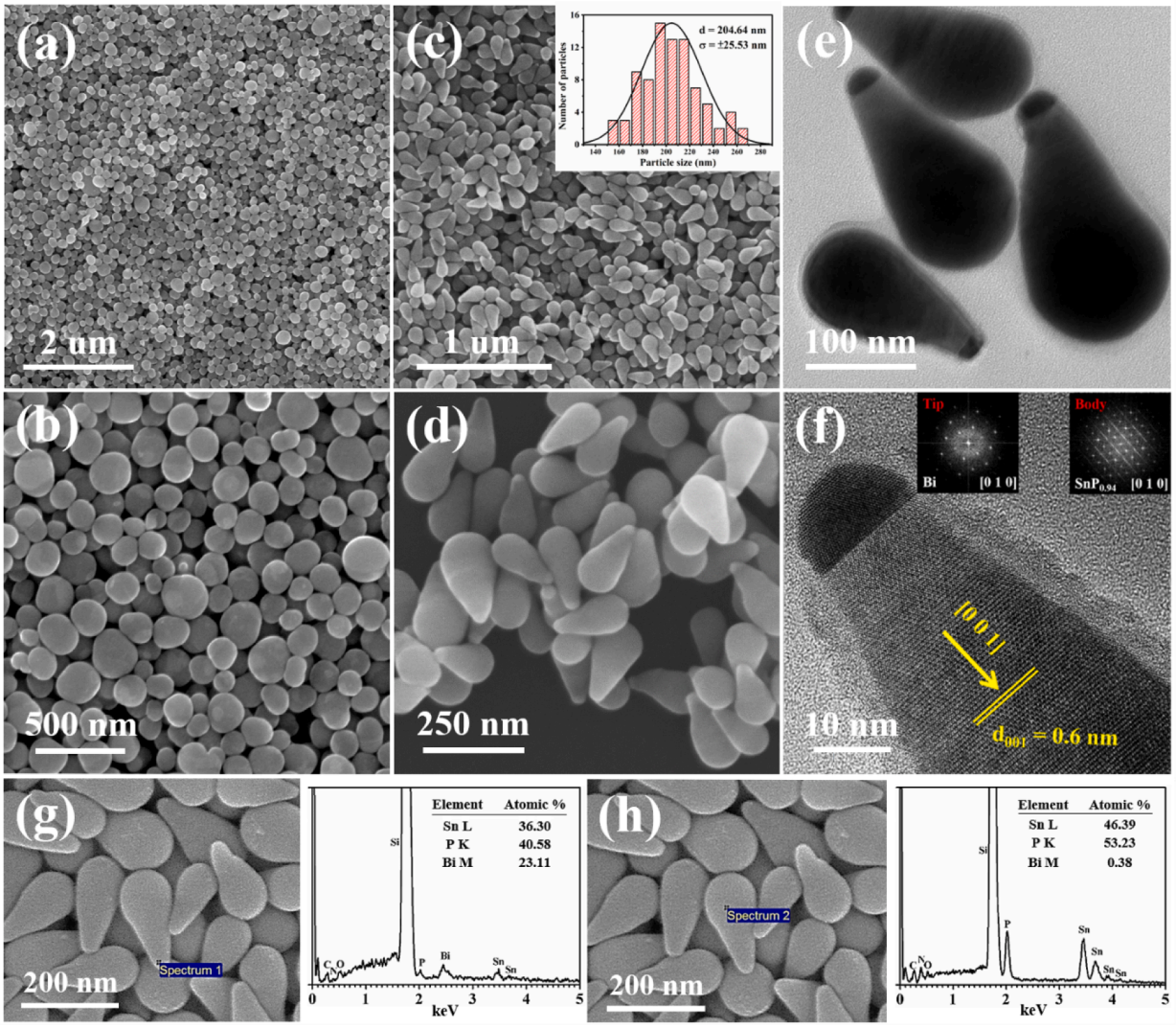


**Fig. 2.** SEM images of (a, b) S-SnP and (c, d) T-SnP with inset of size distribution histogram corresponding to (c). (e) TEM images and (f) the corresponding HRTEM analyses with insets showing fast Fourier transforms of the tip and the body parts of T-SnP. SEM image and corresponding EDS result of (g) the seed part and (h) the body part of T-SnP.

similar characteristics in both discharge/charge profiles. During the first cathodic process, three reduction peaks located around 1.0 and 0.5 V were observed. The former one can be interpreted as irreversible inserting potassium ions with the MWCNT/KB framework (Figure S5). The broad peak in the region of 0.8 to 0.3 V can be regard as the formation of SEI and the conversion alloying process of T-SnP and potassium ions [27]. The following overlapping CV curves show that T-SnP electrode has high reversibility. The electrode activation and SEI formation in the first scan can be confirmed by a further constant current charge and discharge (GCD) test. In Fig. 3b, at a current density of 50 mA $g^{-1}$, the initial discharge and charge capacities of T-SnP are 680.5 and 338.9 mA h $g^{-1}$, and the initial Coulombic efficiency (ICE) is 50.2%. This initial capacity loss can be attributed to the irreversible insertion of potassium ions into the carbon materials and the growth of the SEI layer. Subsequently, the activation of electrode provides a gradual increase in capacity due to more active sites for potassiation. After the 10th cycle, the capacity remained at 393.3 mA h $g^{-1}$ and the Coulombic efficiency was 99.2%. The tough scaffolding of KB and MWCNT improves the stability of the SEI layer, and only 1.0% degradation from the 20th cycle to the 100th cycle. The discharge plateaus of about 1.0 V in the first cathodic cycle may correspond to the cathodic peak in the first cycle of the CV curve. In the meantime, the rate capability and cycling performance of S-SnP, commercial Sn powder, and commercial P powder were also evaluated. In Fig. 3c, the average reversible capacities of T-SnP are 422.8, 377.1, 339.6, 316.9, 301.8, 285.8, 254.3, 219.4, 166.1, and 117.9 mA h $g^{-1}$ at current densities of 50, 100, 250, 500, 750, 1000, 1500, 2500, 5000, 7500 mA $g^{-1}$, which is slightly better than S-SnP electrode. When the current density is restored to 50 mA $g^{-1}$, T-SnP can maintain the same capacity as the initial cycle, which shows that the reversibility is high. At a current density of 500 mA $g^{-1}$, the specific capacity of T-SnP is 298.2 mA h $g^{-1}$, while the S-SnP exhibits a capacity of 101.3 mA h $g^{-1}$ after 180 cycles (Fig. 3d). Obviously, these results indicate that the material morphology will significantly affect the electrochemical performance. The detailed reasons can be obtained from the electrochemical impedance spectroscopy (EIS) test measured in the range of 20 mHz to 100 kHz, as shown in Fig. 3e. The first parallel element of the analog equivalent circuit is regarded as the formation of SEI ($R_{sf}$), and the second parallel element is the charge transfer resistance ($R_{ct}$) that follows the Warburg diffusion process impedance. Without electrode activation, the original semicircles at the high and middle frequency of T-SnP and S-SnP are almost the same in the Nyquist plots. However, after the 10th and 50th cycle, the reduced impedance of T-SnP is superior to that of S-SnP. Moreover, the fitted value of each resistance has been simulated using Zfit software, and the results are

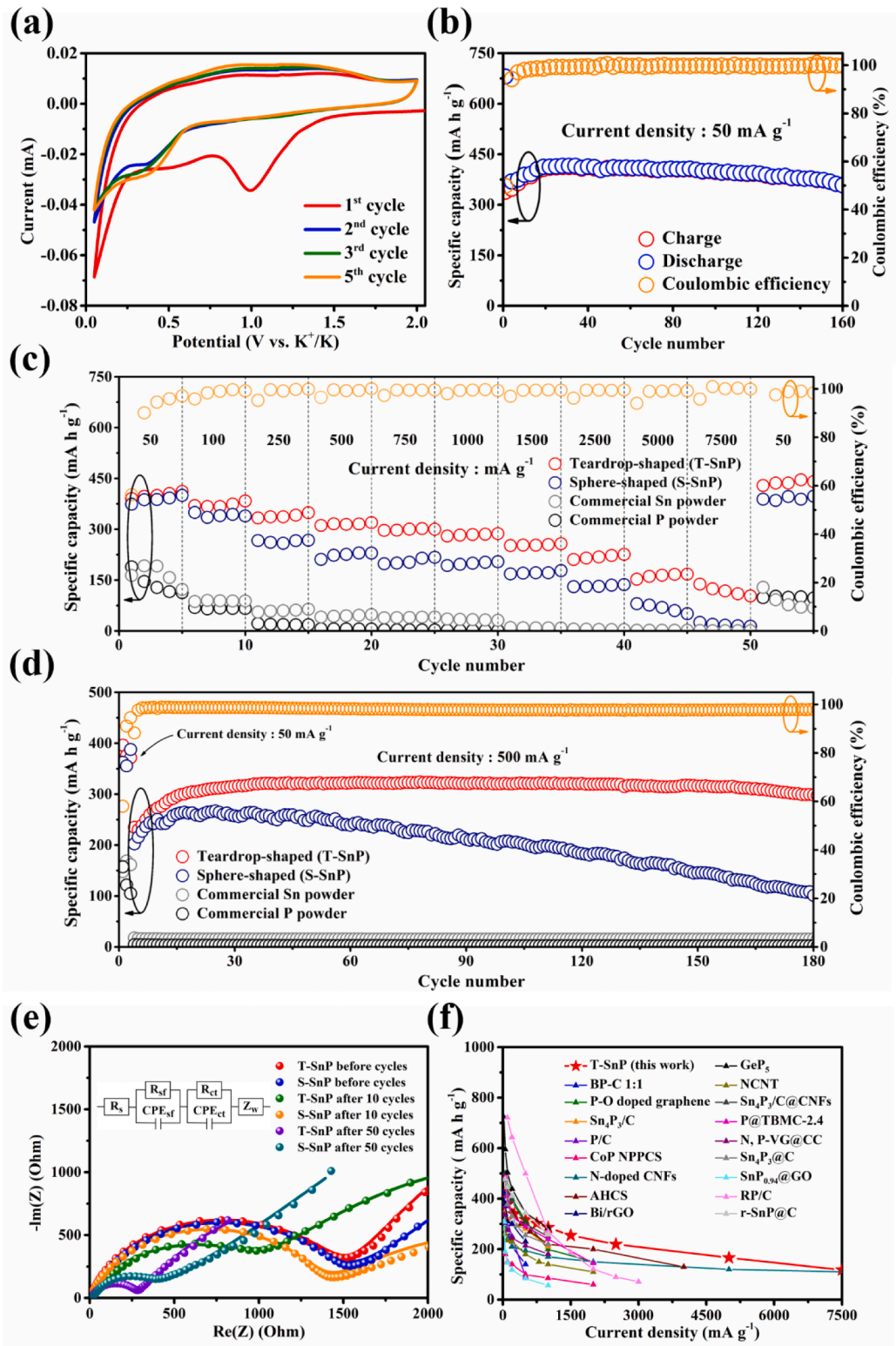


**Fig. 3.** Electrochemical analyses of T-SnP half-cells. (a) CV curves at 0.1 mV $s^{-1}$. (b) Cycling performance at the current density of 50 mA $g^{-1}$. (c) The rate performance at various current densities from 50 to 7500 mA $g^{-1}$ and (d) cycling performance at the current density of 500 mA $g^{-1}$ (first three cycles are 50 mA $g^{-1}$) of T-SnP, S-SnP, commercial Sn powder, and commercial P powder electrode. (e) EIS Nyquist plots of T-SnP and S-SnP in various cycling. (f) Comparison with the rate capability of T-SnP electrode (this work) and previously reported metal phosphides and carbonaceous anodes for PIBs.

shown in Table 1. In both cases, the values of ohmic resistance ($R_s$) are similar in each state, revealing little contribution in performance evolutions. The gradually rising in capacity can be attributed to the increment of active site in electrode/electrolyte interface, displaying the lower $R_{ct}$ and $R_{sf}$ for stable formation of SEI. Particularly, the improvement in T-SnP is more significant. Therefore, from Figure S6, we intend to propose the shape of the T-SnP forming into an anti-pulverization nanostructure with corresponding EDS results (Figure S7), indicating that the volume expansion is stabler. The aggregation of the fragmented S-SnP with KB and SEI makes the $R_{sf}$ larger than T-SnP. The specific capacities at various current densities of T-SnP and other metal phosphides as well as carbonaceous anodes are compared in Fig. 3f and listed in Table S2, displaying the high electrochemical properties of T-SnP. Figure S8 shows the galvanostatic charge–discharge curves of T-SnP and S-SnP, which can correspond to the above-mentioned cycling performance.

**Table 1**
The resistances calculated from EIS Nyquist plots of T-SnP and S-SnP electrodes.

| Electrode | Cycling state | $R_s$ (Ohm) | $R_{sf}$ (Ohm) | $R_{ct}$ (Ohm) |
|---|---|---|---|---|
| T-SnP | Before cycles | 3.496 | 1362 | 9796 |
| | After 10 cycles | 2.974 | 1006 | 674.4 |
| | After 50 cycles | 4.305 | 190.1 | 15.23 |
| S-SnP | Before cycles | 2.309 | 1586 | 9399 |
| | After 10 cycles | 3.933 | 1021 | 1413 |
| | After 50 cycles | 4.671 | 278.3 | 220.6 |

Enhanced by KFSI-based electrolyte in SEI formation, both T-SnP and S-SnP deliver high durability in rate capability derived from the intrinsic layered structure, while S-SnP presents inferior stability and higher resistance in cycling performance. For conversion-alloying anode material, previous studies on the effect of volume expansion during lithiation have proved that the direction of volume change will depend on the orientation of crystal facets [56–58]. Due to the smallest interface energy, the largest spacing provides the largest diffusion channel for lithium ions to the alloy electrode. Therefore, according to this speculation, the hexagonal symmetrical lattice structure of T-SnP indicates that the highest expansion rate will be evenly distributed along the [11-20] directions with lower surface tension to avoid fracture [59] (Fig. 4). Inherent from the shape of nanorod, the lateral tension and mechanical degradation is lower than that of sphere, which can maintain the structural stability and robust ion diffusion tunnels. In accordance with the simulation of crystal structure, as shown in Figure S10, the electrode performance after charge and discharge cycles has been investigated by *ex-situ* TEM to gain a deeper understanding of the electrochemical mechanism based on the morphological effect of $SnP_{0.94}$. Figures S10a to S10d show the clear morphological detail of the T-SnP obtained in the 10th and 50th cycles, respectively. Notably, the tip part of T-SnP is separated from the body part, some of which are wrapped by the SEI layer without aggregation. In addition, the high-angle annular dark field (HAADF) of T-SnP and the corresponding element mapping of T-SnP also show that after the potassiation process, where the tip part decomposes and leaves potassium ions (Figures S10e and S10f). The uniform distributions also show that there is no obvious phase segregation of tin and phosphorus during the cycling test. In Figures S2b-S2i, the *ex-situ* XPS results of T-SnP were performed, which provide more evidence for the phase change during charge and discharge. The disappearance of the P-Sn bond peak indicates that, based on the dual conversion alloying mechanism, a complete dealloying reaction has occurred on the T-SnP electrode. To further determine the overall capacity contribution of Bi, the *ex-situ* XPS was also carried out to confirm the valance state of Bi. However, the low content of Bi in electrode make the rather unclear spectrum after cycling (Figure S9), thus from our perspective, the total capacity of Bi seeds is quite low despite the decomposition with $SnP_{0.94}$.

The electrochemical kinetics of potassium ion storage mechanism and the contribution of the diffusion-controlled process and the surface-controlled process can be analyzed by the redox peaks of CV curve at various purging rates [60] (Fig. 5a). The peak current ($i$) and the scan rate ($v$) follow the equation:

$$i = av^b$$

where the $b$ value can be calculated. For the surface-controlled process, the peak current is proportional to the scan rate, which means that the b value of 1.0. The peak current of diffusion-controlled process is proportional to the square root of the scan rate, indicating that the b value is 0.5. As shown in Fig. 5b, the analysis shows that the b values of the anodic peak and cathodic peak are 0.817 and 0.862, respectively, which indicates that the kinetics of potassium ions in the T-SnP electrode is dominated by both ion diffusion and the capacitive effect. In addition, the contribution to the capacitance in the potential range from 0.05 to 2.0 V can be determined by the following formula:

$$i = k_1 v + k_2 v^{1/2}$$

where $k_1 v$ and $k_2 v^{1/2}$ suggesting the effect comes from both the contribution of surface control and the contribution of diffusion control [61] (Fig. 5c). As shown in Fig. 5d, as the scan rate increases, the capacitive contribution ratio increases from 31.7% of the total potassium ion storage to 62.0%. In Fig. 5e and 5f, the galvanostatic intermittent titration technique (GITT) curves provided a larger potassium ion diffusion coefficient during the charging process of the T-SnP electrode, ranging from $10^{-9}$ to $10^{-10}$ $cm^2$ $s^{-1}$, while the lower range is $10^{-9}$ to $10^{-12}$ $cm^2$ $s^{-1}$ according to the electrode thickness in discharging process (Figure S11). The calculation of GITT formula we used is the following equation:

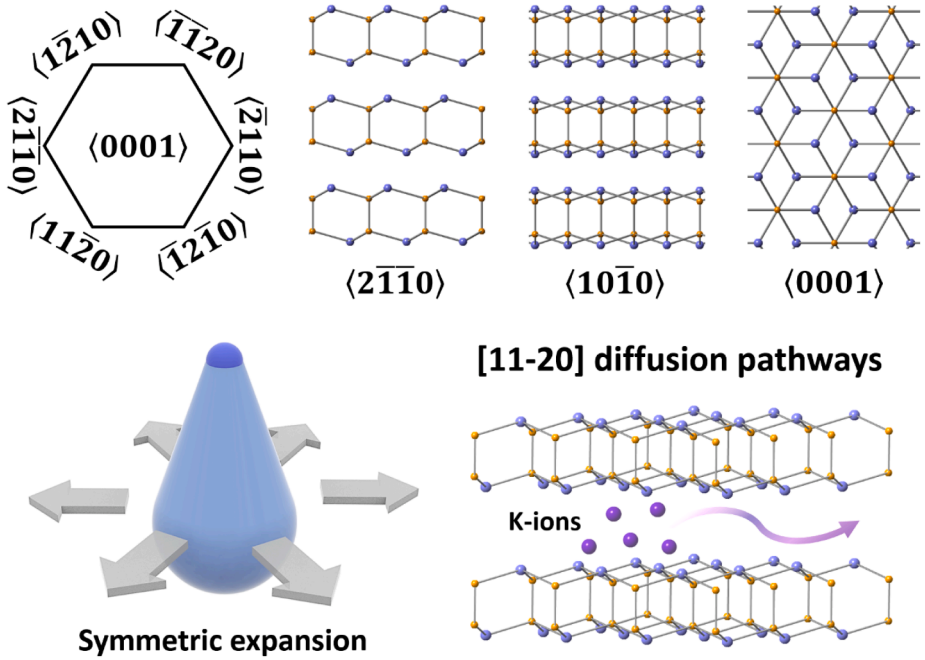


**Fig. 4.** Schematic diagram of the $SnP_{0.94}$ crystallographic orientation of the [11-20] facets and symmetric expansion directions.

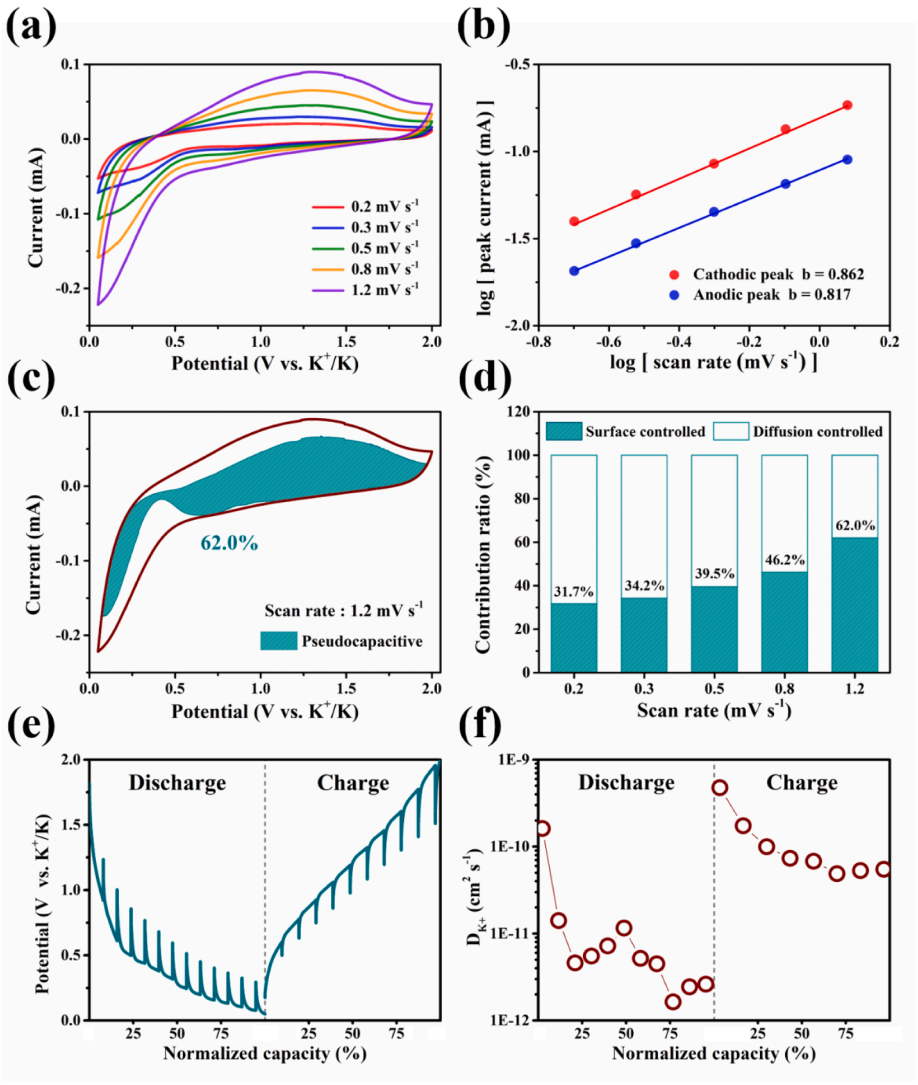


**Fig. 5.** (a) CV curves of T-SnP electrode at different scan rates. (b) Corresponding b values for determination. (c) CV curves at 1.2 mV $s^{-1}$, and the shadowed area exhibited the pseudocapacitive. (d) The contribution ratio of surface-controlled and diffusion-controlled behaviors at different scan rates. (e) GITT curves of T-SnP electrode with 0.5 h current pulse of 100 mA $g^{-1}$ followed by 1 h relaxation and (f) corresponding diffusion coefficient values of current pulses.

$$D = \frac{4}{\pi\tau}\left(\frac{n_m V_m}{S}\right)^2\left(\frac{\Delta E_s}{\Delta E_t}\right)^2 \approx \frac{4}{\pi\tau}(L)^2\left(\frac{\Delta E_s}{\Delta E_t}\right)^2$$

where the $n_m$ and $V_m$ represent the molar number and molar volume of the electrode, while the $S$ means the contacted area of electrode [62]. Therefore, this component can be approximately equal to the thickness of the overall electrode, which can be measured by cross-section SEM images in Figure S11. The $\Delta E_s$ and $\Delta E_t$ are denoted as the voltage change from each pulse and discharge/charge periods. Based on the value of the GITT curve, two plateaus can be found, which can be regard as the potassiation and depotassiation of Sn and P of similar magnitude. The thermodynamic working voltages of each current pulse also reveals that the kinetics of depotassiation state is even more facile, proving that nearly invisible cathodic peaks in CV curve providing softer current change during dealloying process. Moreover, it is confirmed that the calculated high potassium ion diffusion coefficient can provide the electrode materials with high-rate performance.

The T-SnP anode was paired with the PTCDA cathode to assemble a full potassium ion battery to evaluate its feasibility as a PIB anode. The annealed PTCDA for fabrication was prepared by a facile thermal treatment, and the electronic electrochemical performance is shown in Figure S12. Previous studies of PTCDA have revealed the mechanism that the forming of $K_2$PTCDA with a discharge voltage around 2.4 to 2.0 V can deliver a capacity of almost 130 mA h $g^{-1}$ at 1.5 V cut-off voltage [63]. On the basis of the GCD profiles of T-SnP and PTCDA half-cells, the simulation of charge–discharge curves of T-SnP // PTCDA can provide an appropriate voltage range of 0.5 to 3.4 V to prevent FSI-induced corrosion of Al foil at voltage above 4 V [64] (Figure S13). According to half-cell tests above, combining the galvanostatic charge–discharge curves of each half-cell, the loading mass ratio of both electrodes can be properly calculated to evaluate the workability. Figure S14 revealed the mechanism of anode and cathode, indicating that the experimental working voltage is comparable with simulation results. The charge process of T-SnP // PTCDA full cell corresponds to the discharge process of T-SnP half-cell and the charge process of PTCDA half-cell, which means the interaction process of K ions with both electrodes. In Fig. 6a and 6b, the T-SnP // PTCDA full cell can have a specific charge capacity of 419.2 mA h $g^{-1}$ and a specific discharge capacity of 291.1 mA h $g^{-1}$ at the first cycle, with the Coulombic efficiency is 69.5%, at the current density of 50 mA $g^{-1}$. After the 10th cycle, T-SnP // PTCDA full cell can stably exhibit a reversible specific capacity of 180 mA h $g^{-1}$, which indicates that the entire system in the full cell tends to be stable and the T-SnP electrode has been exploited. As shown in Fig. 6c and 6d, the full cell can provide 250, 221, 191, 176, 165, 158 and 150 mA h $g^{-1}$ reversible

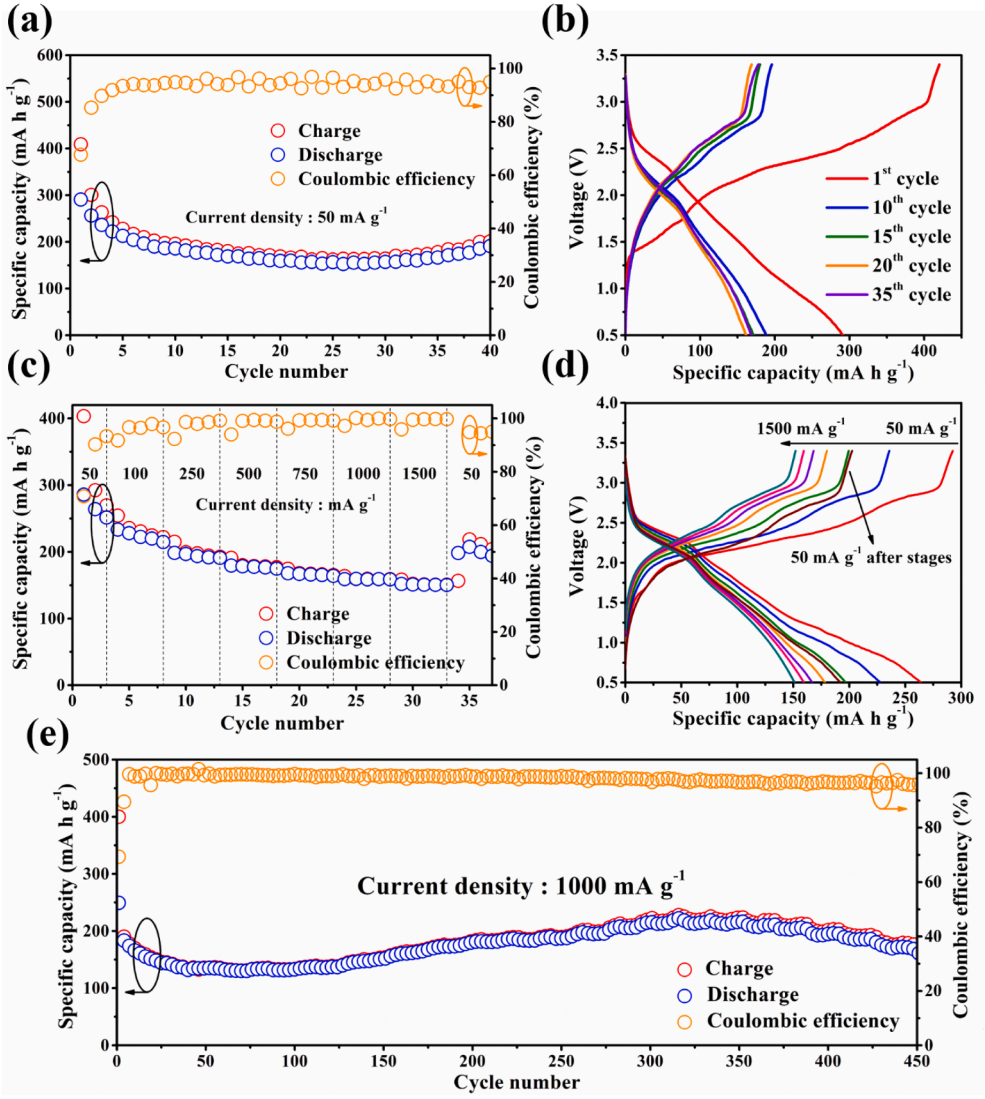


**Fig. 6.** (a, b) Cycling test of the T-SnP // PTCDA full cells at the current density of 50 mA $g^{-1}$ and the corresponding of the voltage profile. (c, d) The rate performance of T-SnP // PTCDA full cell at various current densities from 50 to 1500 mA $g^{-1}$ and the corresponding voltage profiles. (e) Cycling test of the T-SnP // PTCDA full cells at the current density of 1000 mA $g^{-1}$.

capacity at the current density of 50, 100, 250, 500, 750, 1000 and 1500 mA $g^{-1}$, respectively. In addition, the cycle stability of the full cell at a current density of 1000 mA $g^{-1}$ showed long cycle stability during 450 cycles, and the retention rate was 97.59% compare with the 10th cycle, showing significant stability and long-term cycle life (Fig. 6e). For a typical assembly, manual potassium foil should be used as the counter electrode in the Al bag, and both the anode and cathode are both pretreated for 5 cycles in advance, and then reassembled. The T-SnP // PTCDA pouch-type full cell could even light up 55 3 V light emitting diodes (LED) bulbs, as shown in Fig. 7 and Video S1.

In summary, this study of $SnP_{0.94}$ nanomaterials morphology based on SFLS synthesis method has revealed a significant dependence on nanoparticle shapes toward high performance in PIBs. Such surprising nanostructure shape effects have been found for LIBs and SIBs in previous studies, however, this is the first time that teardrop-shaped nanorods have been studied in PIBs. The alloying-dealloying mechanism of the $SnP_{0.94}$ nanomaterials, supported by the lattice-oriented speculation in expansion, can be proposed that $SnP_{0.94}$ has symmetric high-speed ion diffusion tunnels and expansion rate perpendicular to the *c*-axis. The post-mortem analyses on electrodes provided further evidence that T-SnP has a better ability to disperse the surface radial tension with stable SEI formation in contrast to S-SnP, and hence, demonstrating excellent electrochemical performance for potassium ion batteries. It has been proved that the role of $SnP_{0.94}$ morphology, such as T-SnP, plays an important role in adjusting the performance of potassium ion batteries and represents an ideal strategy to further improve the electrochemical properties of unique electrodes.

## Declaration of Competing Interest

The authors declare that they have no known competing financial interests or personal relationships that could have appeared to influence the work reported in this paper.

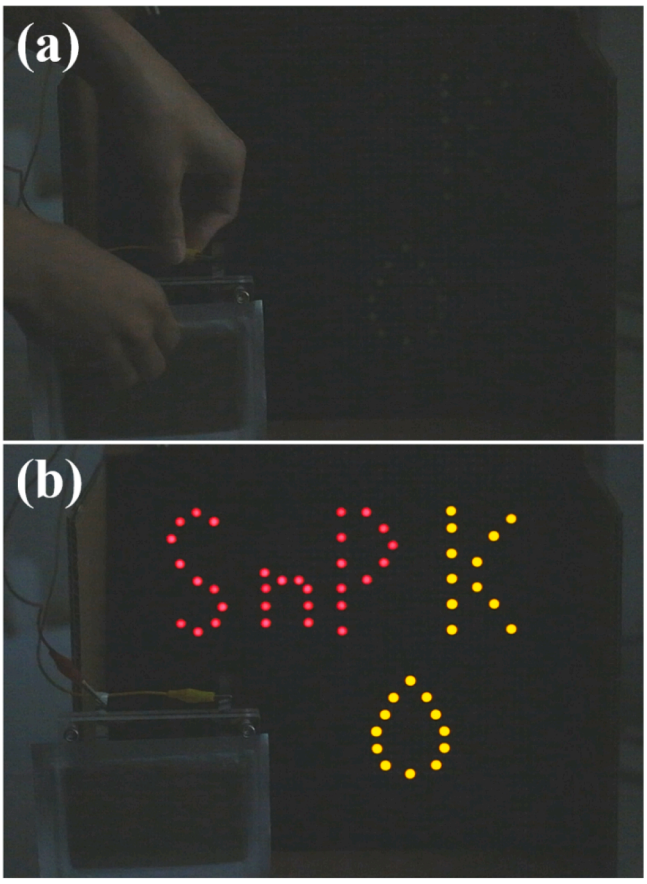


**Fig. 7.** T-SnP // PTCDA pouch-type battery test for lighting up 55 pieces 3 V LED bulbs connected in parallel.

## Acknowledgment

We acknowledge the financial support by the Ministry of Science and Technology through the grants of MOST 108-2636-E-007-013, MOST 108-2622-8-007-016, and MOST 109-2636-E-007-011 and by National Tsing Hua University through the grant of 107Q2708E1.

## References

[1] K. Kubota, M. Dahbi, T. Hosaka, S. Kumakura, S. Komaba, Chem Rec 18 (2018) 459–479.
[2] J.C. Pramudita, D. Sehrawat, D. Goonetilleke, N. Sharma, Adv. Energy Mater. 7 (2017) 1602911.
[3] W. Zhang, Y. Liu, Z. Guo, Sci. Adv. 5 (2019) 7412–7424.
[4] R. Rajagopalan, Y. Tang, X. Ji, C. Jia, H. Wang, Adv. Funct. Mater. 30 (2020) 1909486.
[5] B. Ji, F. Zhang, N. Wu, Y. Tang, Adv. Energy Mater. 7 (2017) 1700920.
[6] Z. Jian, S. Hwang, Z. Li, A.S. Hernandez, X. Wang, Z. Xing, D. Su, X. Ji, Adv. Funct. Mater. 27 (2017) 1700324.
[7] Y. Xie, Y. Chen, L. Liu, P. Tao, M. Fan, N. Xu, X. Shen, C. Yan, Adv. Mater. 29 (2017) 1702268.
[8] Y. Xu, C. Zhang, M. Zhou, Q. Fu, C. Zhao, M. Wu, Y. Lei, Nat. Commun. 9 (2018) 1–11.
[9] W. Wang, J. Zhou, Z. Wang, L. Zhao, P. Li, Y. Yang, C. Yang, H. Huang, S. Guo, Adv. Energy Mater. 8 (2018) 1701648.
[10] J. Yang, Z. Ju, Y. Jiang, Z. Xing, B. Xi, J. Feng, S. Xiong, Adv. Mater. 30 (2018) 1700104.
[11] C. Liu, N. Xiao, H. Li, Q. Dong, Y. Wang, H. Li, S. Wang, X. Zhang, J. Qiu, Chem. Eng. J. 382 (2020), 121759.
[12] X. Yuan, B. Zhu, J. Feng, C. Wang, X. Cai, R. Qin, Chem. Eng. J. 405 (2020), 126897.
[13] X. Wu, Y. Chen, Z. Xing, C.W.K. Lam, S.S. Pang, W. Zhang, Z. Ju, Adv. Energy Mater. 9 (2019) 1900343.
[14] Y. Liu, Z. Tai, Q. Zhang, H. Wang, W.K. Pang, H.K. Liu, K. Konstantinov, Z. Guo, Nano Energy 35 (2017) 36–43.
[15] J. Huang, X. Lin, H. Tan, B. Zhang, Adv. Energy Mater. 8 (2018) 1703496.
[16] J. Zheng, Y. Yang, X. Fan, G. Ji, X. Ji, H. Wang, S. Hou, M.R. Zachariah, C. Wang, Energy Environ. Sci. 12 (2019) 615–623.
[17] J. Ding, H. Zhang, H. Zhou, J. Feng, X. Zheng, C. Zhong, E. Paek, W. Hu, D. Mitlin, Adv. Mater. 31 (2019) 1900429.
[18] Q. Liu, W. Deng, C.-F. Sun, Energy Stor. Mater. 28 (2020) 10–16.
[19] W.C. Chang, J.H. Wu, K.T. Chen, H.Y. Tuan, Adv. Sci. 6 (2019) 1801354.
[20] Y. An, Y. Tian, L. Ci, S. Xiong, J. Feng, Y. Qian, ACS Nano 12 (2018) 12932–12940.
[21] I. Sultana, M.M. Rahman, T. Ramireddy, Y. Chen, A.M. Glushenkov, J. Mater. Chem. A 5 (2017) 23506–23512.
[22] Y. Wu, H.B. Huang, Y. Feng, Z.S. Wu, Y. Yu, Adv. Mater. 31 (2019) 1901414.
[23] D. Yang, C. Liu, X. Rui, Q. Yan, Nanoscale 11 (2019) 15402–15417.
[24] I. Sultana, M.M. Rahman, Y. Chen, A.M. Glushenkov, Adv. Funct. Mater. 28 (2018) 1703857.
[25] R. Verma, P.N. Didwal, H.-S. Ki, G. Cao, C.-J. Park, A.C.S. Appl, Mater. Interfaces 11 (2019) 26976–26984.
[26] W. Zhang, J. Mao, S. Li, Z. Chen, Z. Guo, J. Am. Chem. Soc. 139 (2017) 3316–3319.
[27] X. Zhao, W. Wang, Z. Hou, G. Wei, Y. Yu, J. Zhang, Z. Quan, Chem. Eng. J. 370 (2019) 677–683.
[28] Y. Kim, H. Hwang, C.S. Yoon, M.G. Kim, J. Cho, Adv. Mater. 19 (2007) 92–96.
[29] J. Liu, S. Wang, K. Kravchyk, M. Ibáñez, F. Krumeich, R. Widmer, D. Nasiou, M. Meyns, J. Llorca, J. Arbiol, J. Mater. Chem. A 6 (2018) 10958–10966.
[30] C. Liu, X. Han, Y. Cao, S. Zhang, Y. Zhang, J. Sun, Energy Stor. Mater. 20 (2019) 343–372.
[31] D. Li, Y. Zhang, Q. Sun, S. Zhang, Z. Wang, Z. Liang, P. Si, L. Ci, Energy Stor. Mater. 23 (2019) 367–374.
[32] B. Li, S. Shang, J. Zhao, D.M. Itkis, X. Jiao, C. Zhang, Z.-K. Liu, J. Song, Carbon 168 (2020) 468–474.
[33] W. Zhang, Z. Wu, J. Zhang, G. Liu, N.-H. Yang, R.-S. Liu, W.K. Pang, W. Li, Z. Guo, Nano Energy 53 (2018) 967–974.
[34] S. Liu, J. Mao, Q. Zhang, Z. Wang, W.K. Pang, L. Zhang, A. Du, V. Sencadas, W. Zhang, Z. Guo, Angew. Chem. Int. Ed. 59 (2020) 3638–3644.
[35] W. Zhang, W.K. Pang, V. Sencadas, Z. Guo, Joule 2 (2018) 1534–1547.
[36] L. Zhang, X. Gu, X. Mao, S. Wen, P. Dai, L. Li, D. Liu, X. Zhao, J. Power Sources 486 (2020), 229373.
[37] C.K. Chan, H. Peng, G. Liu, K. McIlwrath, X.F. Zhang, R.A. Huggins, Y. Cui, Nat. Nanotechnol. 3 (2008) 31–35.
[38] C.K. Chan, R. Ruffo, S.S. Hong, Y. Cui, J. Power Sources 189 (2009) 1132–1140.
[39] M. Ge, J. Rong, X. Fang, C. Zhou, Nano Lett. 12 (2012) 2318–2323.
[40] S.W. Lee, M.T. McDowell, J.W. Choi, Y. Cui, Nano Lett. 11 (2011) 3034–3039.
[41] S.C. Jung, J.W. Choi, Y.-K. Han, Nano Lett. 12 (2012) 5342–5347.
[42] E.D. Cubuk, W.L. Wang, K. Zhao, J.J. Vlassak, Z. Suo, E. Kaxiras, Nano Lett. 13 (2013) 2011–2015.
[43] G. Longoni, M. Fiore, J.-H. Kim, Y.H. Jung, D.K. Kim, C.M. Mari, R. Ruffo, J. Power Sources 332 (2016) 42–50.
[44] S. Liu, J. Feng, X. Bian, J. Liu, H. Xu, Energy Environ. Sci. 9 (2016) 1229–1236.
[45] X. Song, X. Li, Z. Bai, B. Yan, D. Li, X. Sun, Nano Energy 26 (2016) 533–540.
[46] S.A. Klankowski, R.A. Rojeski, B.A. Cruden, J. Liu, J. Wu, J. Li, J. Mater. Chem. A 1 (2013) 1055–1064.
[47] J.-H. Cho, S.T. Picraux, Nano Lett. 13 (2013) 5740–5747.
[48] P.C. Donohue, Inorg. Chem 9 (1970) 335–337.
[49] J. Gullman, J Solid State Chem 87 (1990) 202–207.
[50] V. Tallapally, R.J.A. Esteves, L. Nahar, I.U. Arachchige, Chem. Mater. 28 (2016) 5406–5414.
[51] J. Park, B. Koo, K.Y. Yoon, Y. Hwang, M. Kang, J.-G. Park, T. Hyeon, J. Am. Chem. Soc. 127 (2005) 8433–8440.
[52] R.L. Woo, L. Gao, N. Goel, M.K. Hudait, K.L. Wang, S. Kodambaka, R.F. Hicks, Nano Lett. 9 (2009) 2207–2211.
[53] L. Fan, K. Lin, J. Wang, R. Ma, B. Lu, Adv. Mater. 30 (2018) 1800804.
[54] J. Wang, L. Fan, Z. Liu, S. Chen, Q. Zhang, L. Wang, H. Yang, X. Yu, B. Lu, ACS Nano 13 (2019) 3703–3713.
[55] T. Hosaka, K. Kubota, H. Kojima, S. Komaba, ChemComm 54 (2018) 8387–8390.
[56] Q. Zhang, Y. Cui, E. Wang, J. Phys. Chem. C 115 (2011) 9376–9381.
[57] H. Yang, S. Huang, X. Huang, F. Fan, W. Liang, X.H. Liu, L.-Q. Chen, J.Y. Huang, J. Li, T. Zhu, Nano Lett. 12 (2012) 1953–1958.
[58] G.A. Tritsaris, E. Kaxiras, S. Meng, E. Wang, Nano Lett. 13 (2013) 2258–2263.
[59] S.W. Lee, M.T. McDowell, L.A. Berla, W.D. Nix, Y. Cui, Proc. Natl. Acad. Sci. U.S.A. 109 (2012) 4080–4085.
[60] V. Augustyn, J. Come, M.A. Lowe, J.W. Kim, P.-L. Taberna, S.H. Tolbert, H. D. Abruña, P. Simon, B. Dunn, Nat. Mater. 12 (2013) 518–522.
[61] J. Wang, J. Polleux, J. Lim, B. Dunn, J. Phys. Chem. C 111 (2007) 14925–14931.
[62] S.-B. Huang, Y.-Y. Hsieh, K.-T. Chen, H.-Y. Tuan, Chem. Eng. J. (2020), 127697.
[63] Y. Chen, W. Luo, M. Carter, L. Zhou, J. Dai, K. Fu, S. Lacey, T. Li, J. Wan, X. Han, Nano Energy 18 (2015) 205–211.
[64] D.W. McOwen, D.M. Seo, O. Borodin, J. Vatamanu, P.D. Boyle, W.A. Henderson, Energy Environ. Sci. 7 (2014) 416–426.